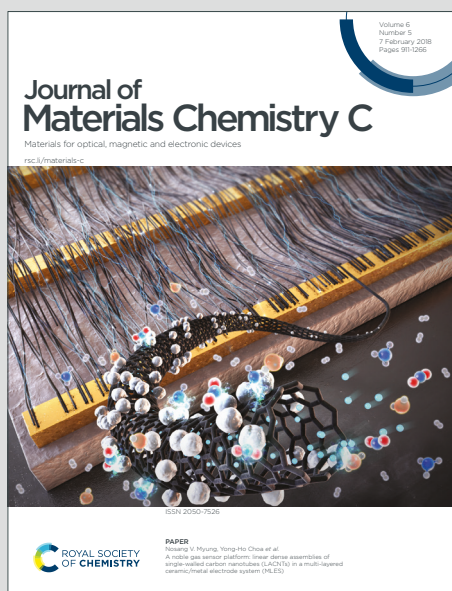


Journal of Materials Chemistry C

Materials for optical, magnetic and electronic devices

Accepted Manuscript

This article can be cited before page numbers have been issued, to do this please use: U. Makhija, V. Kushwaha, N. Prajesh, A. Nag and R. Boomishankar, *J. Mater. Chem. C*, 2025, DOI: 10.1039/D5TC02798E.



This is an Accepted Manuscript, which has been through the Royal Society of Chemistry peer review process and has been accepted for publication.

Accepted Manuscripts are published online shortly after acceptance, before technical editing, formatting and proof reading. Using this free service, authors can make their results available to the community, in citable form, before we publish the edited article. We will replace this Accepted Manuscript with the edited and formatted Advance Article as soon as it is available.

You can find more information about Accepted Manuscripts in the [Information for Authors](#).

Please note that technical editing may introduce minor changes to the text and/or graphics, which may alter content. The journal's standard [Terms & Conditions](#) and the [Ethical guidelines](#) still apply. In no event shall the Royal Society of Chemistry be held responsible for any errors or omissions in this Accepted Manuscript or any consequences arising from the use of any information it contains.

ARTICLE

View Article Online
DOI: 10.1039/D5TC02798E

Piezoelectricity in a mixture of chiral 1D hybrid lead bromide and iodide systems

Urmila Makhija^a, Vikash Kushwaha^a, Neetu Prajesh^a, Angshuman Nag^{a*} and Ramamoorthy Boomishankar^{a*}Received 00th January 20xx,
Accepted 00th January 20xx

DOI: 10.1039/x0xx00000x

Chiral organic–inorganic hybrid perovskites possess inherent structural asymmetry and lattice flexibility, enabling piezoelectric response suitable for energy harvesting and sensing technologies. Here, we introduced a new strategy for the development of a piezoelectric nanogenerator (PENG) constructed from a mixture of two chiral one-dimensional hybrid lead halides, (*R*-MBA)PbBr₃ and (*R*-MBA)PbI₃ (MBA: methybenzylammonium). Individually, both hybrid halide systems exhibit piezoelectric behaviour, but when mixed, the piezoelectric output increases significantly. The highest performance is achieved for the optimized mixed halide mixture: [75 wt% (*R*-MBA)PbBr₃ + 25 wt% (*R*-MBA)PbI₃]. To improve flexibility and mechanical endurance, we incorporated the optimized halide mixture into a polycaprolactone (PCL) polymer matrix. The device with 15 wt% of the optimized halide mixture embedded in PCL demonstrates the highest peak-to-peak voltage of 40.8 V with a power density of 83.1 μW·cm⁻². The halide mixture-PCL composite significantly enhances the device performance, facilitated by its endurance to a higher impact force of 21 N at 8 Hz compared to the neat mixture of hybrid halide salts without PCL (4 N at 6 Hz), leading to a 1.5 times enhancement in the peak-to-peak voltage. Finally, self-powered pressure sensors were fabricated by integrating multiple PENG devices and demonstrated for smart door mat applications. These findings show that physical mixing of chiral hybrid lead halides might be a useful approach to enhance piezoelectric performance.

Introduction

Piezoelectricity arises from non-centrosymmetric crystals, where mechanical deformations can reorient the internal charges, generating an electric field.¹ A chiral crystal automatically fulfils this structural requirement.² In recent times, hybrid organic–inorganic perovskites (HOIPs) have emerged as an interesting semiconductor material with high solar cell efficiency, and incidentally, one can induce chirality in HOIPs.^{3, 4} For example, chiral layered HOIPs like (*R*-MBA)₂PbI₄ and (*S*-MBA)₂PbI₄ (MBA: methybenzylammonium) show an interesting combination of chirality and semiconducting properties.⁵ The chirality is induced from the organic cations to the inorganic framework, often via non-covalent interactions at the organic-inorganic interface. The chiral organic ammonium ions (A-site cation) are typically larger than the void size available for the A-site cation in APbX₃ (X: Cl, Br, I) 3D perovskite structure.^{6–8} So, the chiral HOIPs essentially possess lower-dimensional 2D, 1D or 0D perovskite-like frameworks, where the dimensionality is decided by the connectivity of Pb-X₆ octahedra in 2D, 1D, or 0D (disconnected), respectively.^{9–11} An important advantage of chiral HOIPs lies in the vast flexibility in chemical compositions that is offered by the unlimited choice of A-site organic cations, along with choices in B- and X-site

ions.^{6, 12} In addition, HOIPs possess a low elastic modulus, allowing for greater ionic displacement under lower mechanical forces, compared to rigid ceramic materials.^{13–16} Relying on the huge chemical space and structural tunability, chiral and non-centrosymmetric HOIPs and their derivatives became potential candidates for the exploration of piezoelectric properties.^{11, 17–20}

One of the early studies of piezoelectricity in 2D HOIPs was reported by Du and coworkers, where they reported the structural non-centrosymmetry and piezoelectric response in a series of acene-alkylamine containing compounds like (phenylmethylammonium)₂PbBr₄.²¹ Zhang and coworkers reported an organometallic-based 1D HOIP derivative [(ferrocenylmethyl)trimethylammonium]PbI₃ with a piezoelectric coefficient (*d*₃₃) of ~30 pC/N, along with a narrow bandgap of 2.37 eV.²² A notably high *d*₃₃ of ~1540 pC/N was reported for (TMFM)_x(TMCM)_{1–x}CdCl₃ by making a solid solution of TMFM (trimethylfluoromethyl ammonium) and TMCM (trimethylchloromethyl ammonium) organic A-site cations.²³ Rahmany and coworkers demonstrated a quasi-2D butyl diamine-based perovskite (C₄H₇(NH₃)₂)(CH₃NH₃)₄Pb₅Br₁₆ with a high strain response of 147 pm/V, a unit that indicates the mechanical deformation in picometers per volt of applied electric field.²⁴ These studies highlight the potential of tuning the chemical compositions and structure of HOIPs to achieve piezoelectric platforms with improved performance. Spurred by this, we set out to explore the role of mixing two HOIP derivatives with different halide ions on their piezoelectric We prepared two chiral 1D HOIP derivatives (*R*-MBA)PbBr₃ and (*R*-MBA)PbI₃. Both samples crystallize in the non-centrosymmetric orthorhombic chiral space group *P*2₁2₁. The direct

^a Department of Chemistry, Indian Institute of Science Education and Research (IISER), Pune, Dr. Homi Bhabha Road, Pune – 411008, India, E-mail:

boomi@iiserpune.ac.in, angshuman@iiserpune.ac.in.

Electronic supplementary information (ESI) available: Experimental details, supplementary data, synthesis and characterization of the compounds. CCDC 2472841 and 2472834. See DOI: 10.1039/x0xx00000x



piezoelectric strain coefficient (d_{33}) was measured using the Berlincourt method, yielding a d_{33} value of 0.93 pC/N for (R-MBA)PbBr₃ and 0.85 pC/N for (R-MBA)PbI₃. Interestingly, the d_{33} value increases after mixing the two samples. The mixture with 75 wt% (R-MBA)PbBr₃ and 25 wt% (R-MBA)PbI₃ shows the highest d_{33} value of 5.20 pC/N, along with a peak output voltage of 27.1 V and power density of 5.4 $\mu\text{W}\cdot\text{cm}^{-2}$ under a constant mechanical actuation. The best-performing mixture [75 wt% (R-MBA)PbBr₃ + 25 wt% (R-MBA)PbI₃] was embedded into a polycaprolactone (PCL) matrix to fabricate hybrid halide-polymer composite piezoelectric nanogenerator (PENG) devices with mechanical flexibility. The optimized device generates a peak voltage of 40.8 V, with power and current densities reaching 83.1 $\mu\text{W}\cdot\text{cm}^{-2}$ and 3.5 $\mu\text{A}\cdot\text{cm}^{-2}$, respectively. A full-bridge rectifier-capacitor circuit enabled charge storage of 9.8 μC and an energy output of 4.95 μJ within 400 seconds. A sensor mat application is demonstrated using a parallel array of the PENG devices.

Results and Discussion

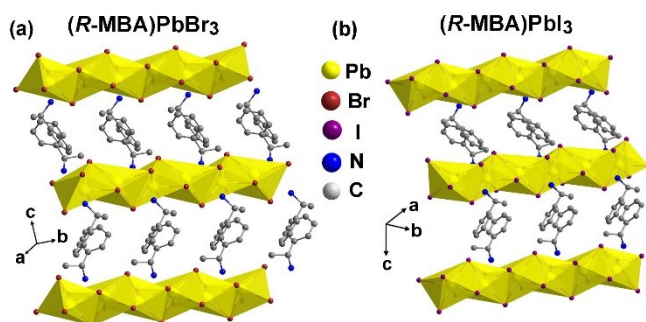


Figure 1. Crystallographic structure diagram of (a) (R-MBA)PbBr₃ and (b) (R-MBA)PbI₃ obtained from SCXRD data at 100 K. The structure comprises one-dimensional chains of lead-halide octahedra with R-MBA cations positioned between them.

White needle shaped crystals of (R-MBA)PbBr₃ and block shaped yellow crystals of (R-MBA)PbI₃ were prepared following different methodologies discussed in the experimental section. SCXRD data analyses of (R-MBA)PbBr₃ and (R-MBA)PbI₃ at 100 K show that both samples crystallize in the orthorhombic $P2_12_12_1$ chiral space group, similar to prior reported structures at 293 K.^{25, 26} The structural refinement parameters for (R-MBA)PbBr₃ and (R-MBA)PbI₃ are listed in Table S1 and Table S2, respectively (ESI). The crystal structure of (R-MBA)PbBr₃ at 100 K (Figure 1a) reveals infinite 1D chains of face-shared [PbBr₆] octahedra aligned along the *a*-axis, bridged by three $\mu^2\text{-Br}^-$ ions. R-MBA cations are positioned above and below these chains, forming a layered arrangement. In (R-MBA)PbBr₃, each cation forms four hydrogen bonds with the [PbBr₆]⁻ unit (Figures S1, ESI). Similar alternate stacking of R-MBA cations with the face-shared lead iodide chains is present in (R-MBA)PbI₃ system (Figure 1b). Hydrogen bonding of (R-MBA)PbI₃ cation with [PbI₆]⁻ unit shows three hydrogen bonds (Figure S2, ESI). The hydrogen bonding parameters for both systems are presented in Tables S3 and S4, respectively (ESI).

The crystallographic unit cell structures of (R-MBA)PbBr₃ and (R-MBA)PbI₃ are determined at 100 K (Figure S3, ESI). The point group symmetry of compounds (R-MBA)PbBr₃ and (R-MBA)PbI₃ is classified as D_2 , which belongs to the orthorhombic system with no inversion symmetry, making these compounds structurally suitable for piezoelectric investigations.²⁷ The unit cell parameter comparison of (R-MBA)PbBr₃ and (R-MBA)PbI₃ at 100 K and at 298 K shows that the lattice shrinks at 100 K without phase change (Table S5, ESI). Comparative analysis of the crystallographic bond parameters for the bromide and iodide analogues indicates a general contraction in both bond lengths and bond angles upon cooling from 298 K to 100 K, (Tables S6 and S7, ESI). This thermally induced structural compression is consistent with reduced lattice dynamics.²⁸

The phase purity in the powder form of (R-MBA)PbBr₃ and (R-MBA)PbI₃ was verified by comparing the PXRD (powder X-ray diffraction) patterns of their ground powder with the simulated powder patterns obtained from the corresponding SCXRD (single crystal X-ray diffraction) data. Figures S4 and S5 (ESI) show a good match of the experimental PXRD and simulated pattern at 293 K. Expectedly, the simulated PXRD patterns obtained from our SCXRD data recorded at 100 K is slightly shifted towards the higher 2 θ value compared to the 293 K simulated data, due to lattice contraction at lower temperatures.²⁶ The TGA (thermogravimetric analysis), DTA (differential thermal analysis) and DSC (differential scanning calorimetry) data (Figure S6a,b ESI) indicate that (R-MBA)PbBr₃ exhibit thermal stability up to a temperature of 493 K. DTA profiles show no distinct thermal events, indicating no structural phase transitions within the stability window; phase stable in the measured temperature range of 123 K to 493 K. Likewise, for (R-MBA)PbI₃, the thermal stability was found up to 486 K, DTA showed no distinct thermal event, and phase stability ranging from 123 K to 486 K (until the decomposition temperature) (Figure S6c,d, ESI). UV-Vis absorption spectra (Figure S7, ESI) of (R-MBA)PbBr₃ and (R-MBA)PbI₃ show sharp absorption edges indicating band gaps of around 369 nm (3.36 eV) and 472 nm (2.63 eV), respectively.

PFM is a non-destructive technique for mapping piezoelectric domains and evaluating local switchable behaviour at the nanometer scale.²⁹ Figures 2a and 2b display the out-of-plane amplitude maps of (R-MBA)PbBr₃ and (R-MBA)PbI₃, respectively. Both images exhibit distinct amplitude contrast across adjacent regions, indicative of the presence of oppositely polarized piezoelectric domains. The significant variations in amplitude signal across neighbouring domains reflect the non-uniform distribution of local piezoelectric activity, likely stemming from intrinsic domain configurations and switching behaviour under the applied AC bias. Figures 2c and 2d show the PFM amplitude hysteresis loops for both (R-MBA)PbBr₃ and (R-MBA)PbI₃ pellets, depicting a classic butterfly-shaped loop associated with piezoelectric behaviour. Both loops are symmetric about the origin, reflecting a typical field-induced piezoelectric strain response. The loops are broader for both (R-MBA)PbBr₃ and (R-MBA)PbI₃, extending over a bias range of ± 200 V and the minima in piezoresponse amplitude indicative of the polarization switch occurring near 0 V. This indicates that both materials exhibit reversible switching with relatively low coercive voltages.



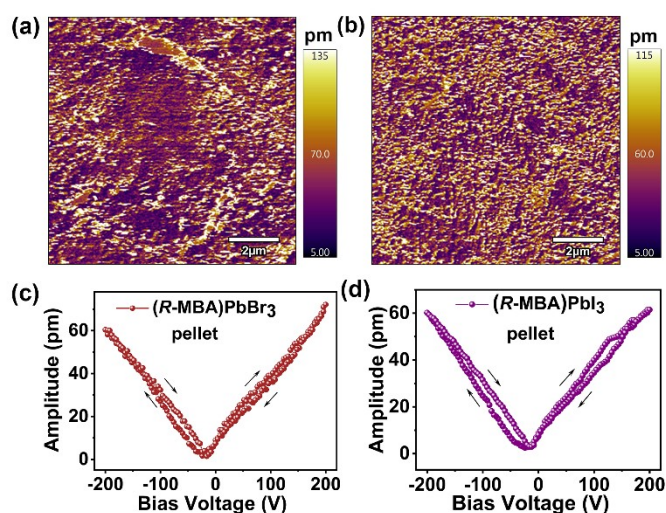


Figure 2. (a) Piezoresponse force microscopy (PFM) images of pellets of (R-MBA)PbBr₃ and (b) (R-MBA)PbI₃. Amplitude signal as a function of the tip bias, representing the local PFM hysteresis loops for (c) (R-MBA)PbBr₃ and (d) (R-MBA)PbI₃ pellets.

To analyse the piezoelectric output, we prepared drop-cast films of (R-MBA)PbBr₃ and (R-MBA)PbI₃, as illustrated in Figure 3a. 200 mg of the finely ground powder sample was mixed with 2 mL hexane, and sonicated for 10 minutes and then kept on stirring for 10 minutes on a heating plate at room temperature to ensure uniform mixing of powders. A double-sided insulating tape was affixed along the edges to define a 2 × 2 cm² area for slurry casting and to prevent electrical short circuits. The resulting slurry was drop-casted onto the adhesive side of the copper tape and the slurry was allowed to dry at ambient temperature until complete evaporation of hexane. The film was subsequently covered with a second layer of copper tape serving as the top electrode, and electrical contacts were established. The assembled device was further encapsulated with Kapton tape. The piezoelectric output performance of the (R-MBA)PbBr₃ and (R-MBA)PbI₃ devices was assessed using a custom-built impact setup.^{30, 31} Measurements were performed under a constant impact force of 4 N at an operating frequency of 6 Hz. The recorded output peak-to-peak voltages (V_{pp}) were 16.4 V and 11.4 V for (R-MBA)PbBr₃ and (R-MBA)PbI₃, respectively (Figure 3b).

To explore any possible role of mixing the two chiral hybrid lead halides on piezoelectric response, we physically mixed x wt% (R-MBA)PbBr₃ and (100- x) wt% (R-MBA)PbI₃, with $x = 100, 75, 50, 25, 0$. The PXRD patterns of these mixtures were compared with the simulated patterns of the end members (Figure S8, ESI). The mixtures show a combination of individual PXRD peaks of end members (R-MBA)PbBr₃ and (R-MBA)PbI₃, without a systematic peak shift with the mixture composition " x ". Instead, the relative intensity of PXRD peaks for (R-MBA)PbBr₃ systematically decreases as the wt% of x (in x wt% (R-MBA)PbBr₃ and (100- x) wt% (R-MBA)PbI₃) decreases. These results show the mixture remains as just a physical mixture, without any significant formation of the alloyed solid solution. Halide ion intermixing (alloying) would have shifted the PXRD peaks, which were found to be absent as observed from Figure S8. The FESEM (field effect scanning electron microscopy) images, along with the

elemental mapping, suggest good distribution of both (R-MBA)PbBr₃ and (R-MBA)PbI₃ in the mixture (Figure S9). DOI: 10.1039/D5TC02798E

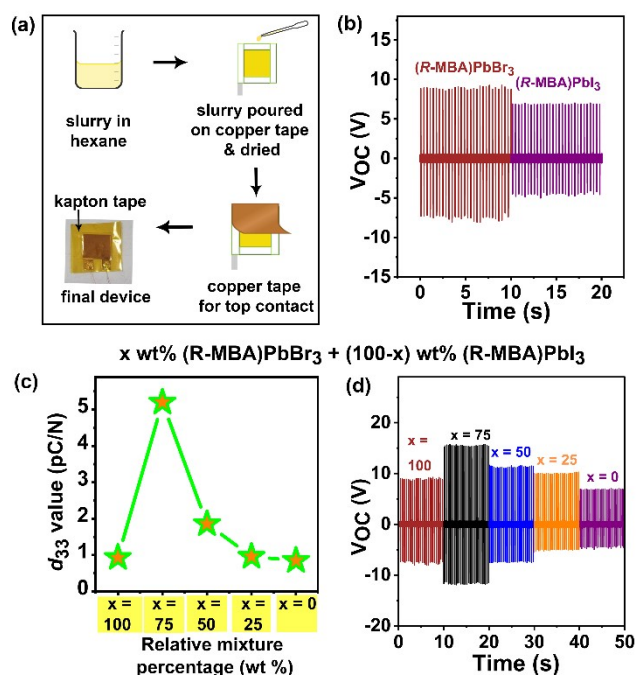


Figure 3. (a) Schematic illustration of the fabrication of neat powder devices of (R-MBA)PbI₃. (b) Comparative output voltage of neat powder devices of (R-MBA)PbBr₃ and (R-MBA)PbI₃ systems, with an area of 2 × 2 cm² at 4 N force and 6 Hz frequency. (c) d_{33} values from pellets of mixtures at 0.25 N tapping force and 110 Hz frequency, and (d) output peak-to-peak voltages (V_{pp}) from devices of mixtures of x wt% (R-MBA)PbBr₃ and (100- x) wt% (R-MBA)PbI₃, with $x = 100, 75, 50, 25$ and 0. The device area for (b) is 2 × 2 cm².

We measured d_{33} response of the pellets of the mixtures, x wt% (R-MBA)PbBr₃ and (100- x) wt% (R-MBA)PbI₃ (Figure 3c and Figure S10, ESI). Interestingly, the d_{33} values change significantly with the mixture composition " x ". The highest d_{33} value of 5.20 pC/N was obtained for $x = 75$, i.e., the mixture with 75 wt% (R-MBA)PbBr₃ and 25 wt% (R-MBA)PbI₃. The other mixtures also show higher d_{33} values compared to the end members $x = 100$ or 0. The lowest d_{33} value of 0.85 pC/N was obtained for pure (R-MBA)PbI₃ ($x = 0$). The increase in d_{33} value after mixing the two samples is an interesting observation, though the microscopic origin of this increase is not yet clear. Probably, the mixture of (R-MBA)PbBr₃ and (R-MBA)PbI₃ helped to align the dipoles in some favourable ways, enhancing the macroscopic piezoelectric polarization (d_{33}).

We further fabricated piezoelectric nanogenerator devices for the measurement to demonstrate the energy harvesting applications of these mixtures. The detailed schematic of the device fabrication using the optimized ($x = 75$) mixture composition, 75 wt% (R-MBA)PbBr₃ and 25 wt% (R-MBA)PbI₃, is illustrated in Figure S11 in the ESI. Similar devices were fabricated using other mixtures as well. The device area was 2 × 2 cm². The recorded output peak-to-peak voltages (V_{pp}) were 16.4 V, 27.1 V, 18.6 V, 14.7 V and 11.4 V for the mixture compositions $x = 100, 75, 50, 25$ and 0, respectively, at 4 N force and 6 Hz frequency. The highest output peak-to-peak voltage



is obtained for $x = 75$, which also shows the highest d_{33} value. The maximum current density and power density of $1.1 \mu\text{A}\cdot\text{cm}^{-2}$ and $5.4 \mu\text{W}\cdot\text{cm}^{-2}$, respectively, were obtained (Figure S12, ESI) for the device with the optimized mixture composition $x = 75$. The load resistance used was $1.1 \text{ M}\Omega$.

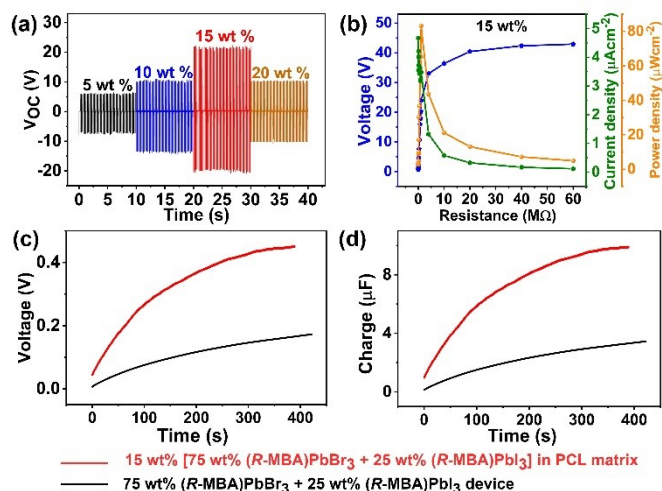


Figure 4. (a) Comparative output voltage of composites after loading different [75 wt% (R-MBA)PbBr₃ + 25 wt% (R-MBA)PbI₃] mixtures in PCL matrix. The device area is $2 \times 2 \text{ cm}^2$. (b) Comparative voltage-drop, power density and calculated current density of the composite device with 15 wt% of the mixture [75 wt% (R-MBA)PbBr₃ + 25 wt% (R-MBA)PbI₃] in PCL matrix. (c) Voltage, and (d) charge stored in a $22 \mu\text{F}$ capacitor using the 15 wt% [75 wt% (R-MBA)PbBr₃ + 25 wt% (R-MBA)PbI₃] mixture in PCL matrix co-plotted with the neat 75 wt% (R-MBA)PbBr₃ + 25 wt% (R-MBA)PbI₃ device. All the measurements for composite devices are done at 21 N force and 8 Hz frequency and for the neat [75 wt% (R-MBA)PbBr₃ + 25 wt% (R-MBA)PbI₃] device at 4 N force and 6 Hz frequency.

Densely packed devices of these lead halide crystal mixtures might face issues of aggregation of crystallites and poor mechanical flexibility, limiting the piezoelectric performance. To address such issues, the piezoelectric crystallites are often embedded into piezo-inactive and flexible polymer matrices.^{32,33} Consequently, we also made polymer composites of these hybrid halides. We got the highest V_{pp} for the chiral hybrid lead halide mixture of composition $x = 75$, [75 wt% (R-MBA)PbBr₃ + 25 wt% (R-MBA)PbI₃]. Therefore, we chose the composite of this mixture with PCL, a polymer known for its piezo-inactivity.³⁴ To this end, polymer composite films incorporating 5, 10, 15, and 20 wt% of the lead-halide mixture ($x = 75$) were prepared with PCL. The schematic synthesis and device fabrication are illustrated (Figure S13, ESI). PXRD pattern of the composite [75 wt% (R-MBA)PbBr₃ + 25 wt% (R-MBA)PbI₃] shows the characteristic peaks for each of the chiral hybrid lead halide compounds, along with new peaks corresponding to the PCL polymer matrix (Figure S14, ESI).³⁵ FESEM images (Figure S15) show that both the piezoelectric lead halide crystallites are embedded in the PCL matrix. The characteristic thickness of the free-standing composite film is $\sim 149 \mu\text{m}$ (Figure S16, ESI).

Importantly, the composite films exhibit good mechanical flexibility, accommodating various bending and folding motions (Figure S17,

ESI). The flexible composite film was used to fabricate the nanogenerator device by attaching adhesive aluminium tapes as the top and bottom electrodes. The devices were then encapsulated with Kapton tape (Figure S18, ESI). The piezoelectric output performances were measured under a constant impact force of 21 N and at an operating frequency of 8 Hz. Figure 4a shows that output peak-to-peak voltages (V_{pp}) of 13.3, 23.8, 40.8, and 20.4 V were observed for the composites with 5, 10, 15, and 20 wt% of the lead halide mixture [75 wt% (R-MBA)PbBr₃ + 25 wt% (R-MBA)PbI₃], respectively. The V_{pp} exhibit an increasing trend with the crystallite loading up to 15 wt%, above which V_{pp} decreases. The increasing output performance up to 15 wt% could be attributed to interfacial polarization (Maxwell–Wagner–Sillars effect).³⁶ Exceeding the optimal crystallite loading threshold probably leads to the aggregation of the piezoelectric domains, suppressing the peak-to-peak voltage. Therefore, maintaining an optimal balance of piezoelectric filler content spread throughout the piezo-inactive matrix is desired for maximum output performance in piezoelectric nanogenerator applications.³⁷ Figure 4b shows that the maximum current and power densities of $3.5 \mu\text{A}\cdot\text{cm}^{-2}$ and $83.1 \mu\text{W}\cdot\text{cm}^{-2}$, respectively, were achieved for the 15 wt% loading of the lead halide mixture [75 wt% (R-MBA)PbBr₃ + 25 wt% (R-MBA)PbI₃] in the PCL matrix, at a resistance of $1.1 \text{ M}\Omega$.

To assess and compare the energy harvesting performance of the piezoelectric nanogenerators, capacitor charging experiments were conducted using a $22 \mu\text{F}$ capacitor for both the polymer composite devices and the neat halide mixture. The alternating current (AC) output from each device was rectified using a full-wave bridge rectifier (Figure S19, ESI) to enable direct current (DC) charging of the capacitor. As shown in the co-plotted voltage-time curves (Figure 4c), the 15 wt% halide mixture polymer composite device comprising 15 wt% of [75 wt% (R-MBA)PbBr₃ + 25 wt% (R-MBA)PbI₃] in a PCL matrix exhibited enhanced voltage output compared to the neat halide mixture. The voltage across the capacitor increased non-linearly, consistent with dielectric charging behaviour reaching approximately $\sim 0.47 \text{ V}$ at 380 s for the composite device, whereas the neat halide mixture device reached $\sim 0.33 \text{ V}$ at 400 s. This higher voltage accumulation highlights improved energy conversion and charge transfer efficiency in the composite system. The corresponding charge accumulation curves (Figure 4d) further validate this difference. The total accumulated charge for the composite device was $\sim 9.8 \mu\text{C}$, greater than the $\sim 3.5 \mu\text{C}$ obtained for the neat halide mixture device under similar charging conditions.

To further evaluate the practical utility of the harvested energy, the stored energy in a $22 \mu\text{F}$ capacitor was calculated for both devices using the equation $E = 0.5 \times CV^2$, where C is the capacitance ($22 \mu\text{F}$) and V is the voltage across the capacitor (Figure S20a and b, ESI). For the neat [75 wt% (R-MBA)PbBr₃ + 25 wt% (R-MBA)PbI₃] device, the capacitor reached a voltage of $\sim 0.33 \text{ V}$ at 400 s, resulting in a stored energy of approximately $1.20 \mu\text{J}$. In contrast, the 15 wt% [75 wt% (R-MBA)PbBr₃ + 25 wt% (R-MBA)PbI₃]-PCL composite device reached a higher voltage of $\sim 0.47 \text{ V}$ at 380 s, translating to an energy storage of $4.95 \mu\text{J}$. The polymer composite device stored more than double the



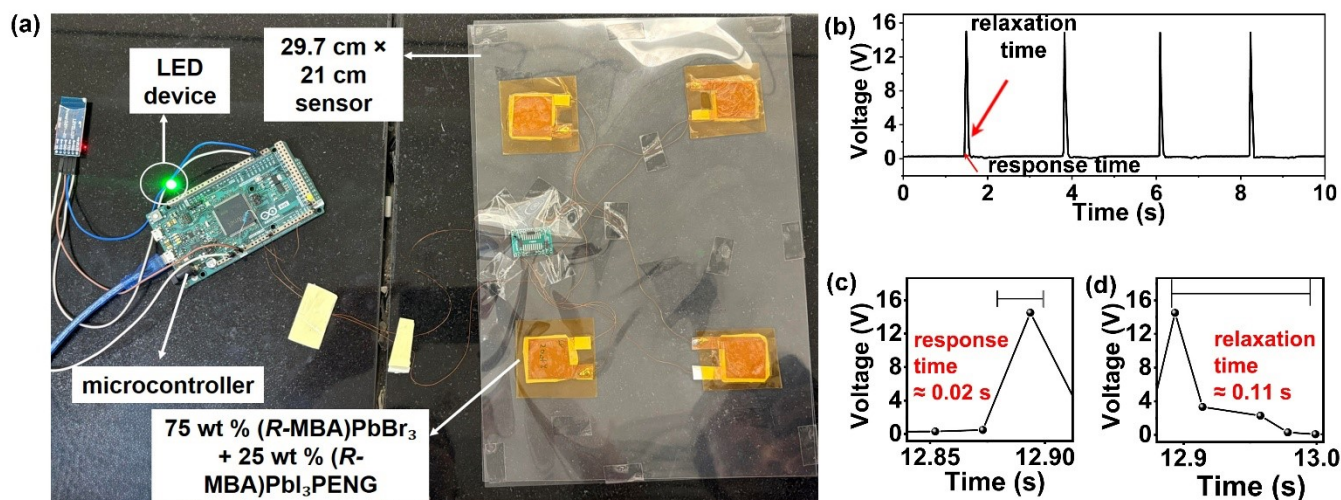


Figure 5. (a) Photograph of the assembled sensor with four 15 wt% high-performing PENG devices between polyethylene terephthalate (PET) sheets. (b) Rectified voltage responses generated by the self-powered sensor during hand-tapping loading and unloading cycles. (c) and (d) Enlarged view of the curves in panel b, showing the response and relaxation times, respectively.

energy compared to the neat halide mixture device under similar conditions. The enhanced energy storage capability of the composite device can be attributed to improved mechanical flexibility and better dielectric properties imparted by the polymer matrix, which facilitate more efficient strain-to-charge conversion and retention.³⁸

The piezoelectric output performance of the chiral hybrid lead halide mixture [75 wt% (R-MBA)PbBr₃ + 25 wt% (R-MBA)PbI₃] before and after embedding (15 wt%) into the PCL matrix is shown in Table S8 of the ESI. The force and the frequency applied for the neat chiral hybrid lead halide mixture device are 4 N at 6 Hz. Forces above 4 N caused film delamination, indicating the mechanical limit of the device. A higher impact force of 21 N at 8 Hz could be applied to all the chiral hybrid lead halide mixture-PCL composite devices. With this higher impact force, the 15 wt% [75 wt% (R-MBA)PbBr₃ + 25 wt% (R-MBA)PbI₃]-PCL composite device clearly performs significantly better, and therefore, is more suitable for applications.

To demonstrate the feasibility of the piezoelectric nanogenerator (PENG) sensor, a prototype smart door mat pressure sensor was designed by integrating multiple PENG devices. The fabricated sensor array consisted of four individual 15 wt% halide mixture [75 wt% (R-MBA)PbBr₃ + 25 wt% (R-MBA)PbI₃]-PCL polymer composite PENG units, securely mounted on a 30 cm × 21 cm flexible polyethylene terephthalate (PET), as illustrated in Figure 5a, and in the supporting video. The circuit diagram is demonstrated in Figure S21. As shown in Figure 5b, a simple hand tapping generates an instantaneous output voltage of approximately 14 V. The generated voltage from the piezoelectric devices was consolidated using a full-wave bridge rectifier. The rectified DC signals were routed to a microcontroller, which served as the central processing unit of the sensing system. The microcontroller continuously monitored the incoming voltages

via its built-in analog-to-digital converter channels, real-time digital processing, and data transmission. In addition to triggering a digital output (specifically, the illumination of a light-emitting diode, LED), the microcontroller was also interfaced with software logic designed for user-interactive decision-making, as has been demonstrated in the supporting video.

The entire sensor surface functioned as a pressure-responsive detector. The measured response time of 0.03 s and relaxation time of 0.11 s suggest rapid detection and recovery, as shown in Figures 5c and 5d. The fast response allows for quick voltage generation upon mechanical impact, while the short relaxation time ensures continuous operation without lag. The response time (~0.02 s) is shorter than the relaxation time (~0.11 s) since it is governed by rapid elastic polarization under stress, whereas relaxation is limited by comparatively slower dipole and charge redistribution processes.³⁹ The preliminary demonstration of the PENG device-based sensor's high voltage output and quick response shows its potential applications in smart security systems, pressure-sensitive interfaces, and human-machine interactions. The integration with existing IoT networks and automation frameworks further enhances the practical utility of such devices. It is noteworthy that, unlike conventional sensors, which require external power sources, this self-powered system operates solely through mechanical energy conversion.

Conclusion

This study demonstrates piezoelectric nanogenerators using 1D chiral hybrid lead halides, (R-MBA)PbBr₃ and (R-MBA)PbI₃. Individually, both samples show piezoelectric device response, but the output enhances significantly when the two samples are mixed.



ARTICLE

Journal Name

The optimized chiral hybrid lead halide mixture with 75 wt% (*R*-MBA)PbBr₃ + 25 wt% (*R*-MBA)PbI₃ shows the highest output. Building on this, a flexible device was fabricated by embedding the optimal chiral hybrid lead halide mixture into a PCL matrix. This composite not only enhanced the output responses but also enabled mechanical durability and flexibility. The final optimised composite device, 15 wt% of halide mixture [75 wt% (*R*-MBA)PbBr₃ + 25 wt% (*R*-MBA)PbI₃] in PCL, was integrated into a smart doormat sensor, capable of detecting human footfalls and generating a response signal. The work highlights the impact of mixing lead halide salts in enhancing piezoelectric response. It also demonstrates the practical feasibility of using such hybrid systems in real-world, self-powered sensing applications. This approach opens new avenues for designing efficient piezoelectric devices using compositionally tunable, chiral hybrid lead halides.

Author contributions

R. B., A. N., U. M., N. P. and V.K. designed the project. R. B. directed the project. U. M. prepared the samples and did the structural characterization. U.M. and V.K. performed the electrical measurements. U.M., A.N. and R. B. wrote the original manuscript. V.K. and N. P. reviewed and edited the manuscript. All the authors discussed the results and contributed sincerely to the preparation of the manuscript.

Data availability

The data that support the findings of this study are available on request from the corresponding author upon reasonable request.

Conflicts of interest

There are no conflicts to declare.

Acknowledgements

This work was supported by SERB, India, via Grant No. CRG/2023/000582 (R. B.), SB/SJF/2020-21/02 (A. N.), CRG/2022/001199 (A. N.) and IISER-Pune. R. B. thanks SERB, India, for the Science and Technology Award for Research (STAR) via Grant No. STR/2021/000016. U.M. thanks UGC and V.K. thanks CSIR, India, for the fellowship. The authors thank Vijay Krishna Mistari and acknowledge BIO-AFM (BSBE)–IRCC BIO Atomic Force Microscopy (BIO-AFM) Central Facility of I. I. T. Bombay for providing PFM data. The authors thank the Department of Science and Technology (FIST program, SR/FST/CS-II/2019/105) for the powder X-ray diffraction facility.

References:

1. K. S. Gerace, J. C. Mauro and C. A. Randall, *J. Am. Ceram. Soc.*, 2021, **104**, 1915-1944.
2. G. H. Fecher, J. Kübler and C. Felser, *Materials*, 2022, **15**, 5812-5844.
3. W. Li, Z. Wang, F. Deschler, S. Gao, R. H. Friend and A. K. Cheetham, *Nat. Rev. Mater.*, 2017, **2**, 16099-16116.
4. Y. Dong, Y. Zhang, X. Li, Y. Feng, H. Zhang and J. Xu, *Small*, 2019, **15**, 1902237-1902255. DOI: 10.1039/D5TC02798E
5. J. Ahn, E. Lee, J. Tan, W. Yang, B. Kim and J. Moon, *Materials Horizons*, 2017, **4**, 851-856.
6. X. Li, J. M. Hoffman and M. G. Kanatzidis, *Chem. Rev.*, 2021, **121**, 2230-2291.
7. Y. Liu, C. Wang, Y. Guo, L. Ma, C. Zhou, Y. Liu, L. Zhu, X. Li, M. Zhang and G. Zhao, *J. Mater. Chem. C*, 2020, **8**, 5673-5680.
8. T. Dutta, D. Swain and A. Nag, *Angew. Chem. Int. Ed.*, 2025, **137**, e202422550.
9. X. Li, S. Aftab, S. Hussain, F. Kabir, A. M. A. Henaish, A. G. Al-Sehemi, M. R. Pallavolu and G. Koyyada, *J. Mater. Chem. A*, 2024, **12**, 4421-4440.
10. Y. Liu, S. Yuan, H. Zheng, M. Wu, S. Zhang, J. Lan, W. Li and J. Fan, *Adv. Energy Mater.*, 2023, **13**, 2300188.
11. R. S. Muddam, S. Wang, N. P. M. J. Raj, Q. Wang, P. Wijesinghe, J. Payne, M. S. Dyer, C. Bowen and L. K. Jagadamma, *Adv. Funct. Mater.*, 2025, **35**, 2425192.
12. J.-W. Lee, S. Tan, S. I. Seok, Y. Yang and N.-G. Park, *Science*, **375**, eabj1186.
13. A. K. Keshri, S. R. Bakshi, Y. Chen, T. Laha, X. Li, C. Levy and A. Agarwal, *Surf. Eng.*, 2009, **25**, 270-275.
14. Q. Tu, I. Spanopoulos, E. S. Vasileiadou, X. Li, M. G. Kanatzidis, G. S. Shekhawat and V. P. Dravid, *ACS Appl. Mater. Interfaces*, 2020, **12**, 20440-20447.
15. H. Gao, W. Wei, L. Li, Y. Tan and Y. Tang, *The J. Phys. Chem. C*, 2020, **124**, 19204-19211.
16. D. K. Khatua and S.-J. Kim, *J. Mater. Chem. C*, 2022, **10**, 2905-2924.
17. Y. Qin, F.-F. Gao, S. Qian, T.-M. Guo, Y.-J. Gong, Z.-G. Li, G.-D. Su, Y. Gao, W. Li, C. Jiang, P. Lu and X.-H. Bu, *ACS Nano*, 2022, **16**, 3221-3230.
18. T. Vijayakanth, D. J. Liptrot, E. Gazit, R. Boomishankar and C. R. Bowen, *Adv. Funct. Mater.*, 2022, **32**, 2109492.
19. Z. Zhang, Y. Zhang, Y. Zhao, M. Zhao, R. Zhang, J. Guo, F. An and X. Sun, *J. Mater. Chem. C*, 2023, **11**, 1401-1408.
20. R. S. Muddam and L. K. Jagadamma, *J. Mater. Chem. C*, 2025, **13**, 10488-10506.
21. K.-z. Du, Q. Tu, X. Zhang, Q. Han, J. Liu, S. Zauscher and D. B. Mitzi, *Inorg. Chem.*, 2017, **56**, 9291-9302.
22. Z.-X. Zhang, H.-Y. Zhang, W. Zhang, X.-G. Chen, H. Wang and R.-G. Xiong, *J. Am. Chem. Soc.*, 2020, **142**, 17787-17794.
23. W.-Q. Liao, D. Zhao, Y.-Y. Tang, Y. Zhang, P.-F. Li, P.-P. Shi, X.-G. Chen, Y.-M. You and R.-G. Xiong, *Science*, 2019, **363**, 1206-1210.
24. S. Rahmany, A. Shpatz Dayan, M. Wierzbowska, A. J. Ong, Y. Li, S. Magdassi, A. I. Y. Tok and L. Etgar, *ACS Energy Letters*, 2024, **9**, 1527-1536.
25. D. G. Billing and A. Lemmerer, *CrystEngComm*, 2006, **8**, 686-695.
26. Y. Dang, X. Liu, Y. Sun, J. Song, W. Hu and X. Tao, *J. Phys. Chem. Lett.*, 2020, **11**, 1689-1696.
27. H.-Y. Zhang, X.-G. Chen, Y.-Y. Tang, W.-Q. Liao, F.-F. Di, X. Mu, H. Peng and R.-G. Xiong, *Chem. Soc. Rev.*, 2021, **50**, 8248-8278.
28. J. Zhao, X. Liu, Z. Wu, B. Ibrahim, J. Thieme, G. Brocks, S. Tao, L. J. Bannenberg and T. J. Savenije, *Adv. Funct. Mater.*, 2024, **34**, 2311727.
29. A. Gruverman, M. Alexe and D. Meier, *Nat. Comm.*, 2019, **10**, 1661.



30. S. Sahoo, N. Deka, V. Kushwaha, V. B. Gadagin, J. K. Zaręba and R. Boomishankar, *J. Mater. Chem. C*, 2025, **13**, 9294-9299.
31. V. Kushwaha, N. Prajesh, A. Gopal, S. Sahoo, S. Deswal, A. Kirana, K. Shanmuganathan, J. K. Zaręba and R. Boomishankar, *J. Mater. Chem. A*, **13**, 2025, 22574-22582.
32. L. Li, L. Han, H. Hu and R. Zhang, *Mater. Adv.*, 2023, **4**, 726-746.
33. A. Kumar, K. Das and A. Roy, *Sens. Actuators A Phys.*, 2024, **376**, 115609.
34. S. Sahoo, R. Panday, P. Kothavade, V. B. Sharma, A. Sowmiyanarayanan, B. Praveenkumar, J. K. Zaręba, D. Kabra, K. Shanmuganathan and R. Boomishankar, *ACS Appl. Mater. Interfaces*, 2024, **16**, 26406-26416.
35. I. García-Casas, A. Montes, D. Valor, C. Pereyra and E. J. Martínez de la Ossa, *Polymers*, 2019, **11**, 1390.
36. K. J. Andrew, *J. Phys. D: Appl. Phys.*, 1999, **32**, R57-R70.
37. R. Ding, H. Liu, X. Zhang, J. Xiao, R. Kishor, H. Sun, B. Zhu, G. Chen, F. Gao, X. Feng, J. Chen, X. Chen, X. Sun and Y. Zheng, *Adv. Funct. Mater.*, 2016, **26**, 7708-7716.
38. D. Singh, A. Choudhary and A. Garg, *ACS Appl. Mater. Interfaces*, 2018, **10**, 2793-2800.
39. N. Prajesh, V. Kushwaha, D. R. Naphade, B. Praveenkumar, J. K. Zaręba, T. D. Anthopoulos and R. Boomishankar, *ACS Appl. Energy Mater.*, 2025, **8**, 4648-4655.

View Article Online
DOI: 10.1039/D5TC02798E



Data availability statement

View Article Online
DOI: 10.1039/D5TC02798E

Experimental details, supplementary data, synthesis, and characterization of the compounds are included in the supplementary information. Crystallographic data have been submitted to CCDC under 2472841 and 2472834.

